catalysts

MDPI

Article

Modulation of the Bifunctional Cr^{VI} to Cr^{III} Photoreduction and Adsorption Capacity in Zr^{IV} and Ti^{IV} Benchmark Metal-Organic Frameworks

Paula G. Saiz [1,2,*,†], Ainara Valverde [1,3,*,†], Bárbara Gonzalez-Navarrete [4,†], Maibelin Rosales [4], Yurieth Marcela Quintero [4], Arkaitz Fidalgo-Marijuan [1,2], Joseba Orive [5], Ander Reizabal [1,3], Edurne S. Larrea [6,7], María Isabel Arriortua [1,2], Senentxu Lanceros-Méndez [1,8], Andreina García [4,9] and Roberto Fernández de Luis [1,*]

1 BCMaterials, Basque Center for Materials, Applications and Nanostructures, UPV/EHU Science Park, 48940 Leioa, Spain; arkaitz.fidalgo@bcmaterials.net (A.F.-M.); ander.reizabal@bcmaterials.net (A.R.); maribel.arriortua@ehu.es (M.I.A.); Senentxu.lanceros@bcmaterials.net (S.L.-M.)
2 Department of Geology, Science and Technology Faculty, University of the Basque Country (UPV/EHU), Barrio Sarriena s/n, Leioa, 48940 Bizkaia, Spain
3 Macromolecular Chemistry Group (LABQUIMAC), Department of Physical Chemistry, Faculty of Science and Technology, University of the Basque Country (UPV/EHU), Barrio Sarriena s/n, 48940 Leioa, Spain
4 Advanced Mining Technology Center (AMTC), University of Chile, Av. Tupper 2007 (AMTC Building), 8370451 Santiago, Chile; barbara.gonzalez152@hotmail.com (B.G.-N.); maibe.rosales@gmail.com (M.R.); yurieth.mar@gmail.com (Y.M.Q.); andreina.garcia@amtc.cl (A.G.)
5 Department of Chemical Engineering, Biotechnology and Materials, Facultad de Ciencias Físicas y Matemáticas, Universidad de Chile, Av. Beauchef 851, 8370451 Santiago, Chile; joseba.orive@ing.uchile.cl
6 Le Studium Research Fellow, Loire Valley Institute for Advanced Studies, 1 Rue Dupanloup, 45000 Orléans, France; edurne.serrano@ehu.eus
7 CEMHTI—UPR3079 CNRS, 1 avenue de la Recherche Scientifique, 45100 Orléans, France
8 IKERBASQUE, Basque Foundation for Science, 48009 Bilbao, Spain
9 Mining Engineering Department, University of Chile, Av. Tupper 2069, 8370451 Santiago, Chile
* Correspondence: paula.gonzalez@bcmaterials.net (P.G.S.); ainara.valverde@bcmaterials.net (A.V.); roberto.fernandez@bcmaterials.net (R.F.d.L.); Tel.: +34-946-12-88-11 (P.G.S & A.V. & R.F.d.L.)
† These authors have contributed equally to the development of the work.

Abstract: The presence of hexavalent chromium water pollution is a growing global concern. Among the currently applied technologies to remove Cr^{VI}, its adsorption and photocatalytic reduction to Cr^{III} less mobile and toxic forms are the most appealing because of their simplicity, reusability, and low energy consumption. However, little attention has been paid to bifunctional catalysts, that is, materials that can reduce Cr^{VI} to Cr^{III} and retain both hexavalent and trivalent chromium species at the same time. In this work, the dual Cr^{VI} adsorption–reduction capacity of two iconic photoactive water-stable zirconium and titanium-based metal–organic frameworks (MOFs) has been investigated: UiO-66-NH_2 and MIL-125. The bifunctionality of photoactive MOFs depends on different parameters, such as the particle size in MIL-125 or organic linker functionalization/defective positions in UiO-66 type sorbents. For instance, the presence of organic linker defects in UiO-66 has shown to be detrimental for the chromium photoreduction but beneficial for the retention of the Cr^{III} phototransformed species. Both compounds are able to retain from 90 to 98% of the initial chromium present at acidic solutions as well as immobilize the reduced Cr^{III} species, demonstrating the suitability of the materials for Cr^{VI} environmental remediation. In addition, it has been demonstrated that adsorption can be carried out also in a continuous flux mode through a diluted photoactive MOF/sand chromatographic column. The obtained results open the perspective to assess the bifunctional sorption and photoreduction ability of a plethora of MOF materials that have been applied for chromium capture and photoreduction purposes. In parallel, this work opens the perspective to develop specific chemical encoding strategies within MOFs to transfer this bifunctionality to other related water remediation applications.

Keywords: metal–organic frameworks; photocatalysis; chromium; photoreduction; adsorption

Citation: G. Saiz, P.; Valverde, A.; Gonzalez-Navarrete, B.; Rosales, M.; Quintero, Y.M.; Fidalgo-Marijuan, A.; Orive, J.; Reizabal, A.; Larrea, E.S.; Arriortua, M.I.; et al. Modulation of the Bifunctional Cr^{VI} to Cr^{III} Photoreduction and Adsorption Capacity in Zr^{IV} and Ti^{IV} Benchmark Metal-Organic Frameworks. *Catalysts* **2021**, *11*, 51. https://doi.org/10.3390/catal11010051

Received: 25 November 2020
Accepted: 18 December 2020
Published: 1 January 2021

1. Introduction

Photocatalytic reduction of hexavalent chromium is becoming an environmentally friendly and easily applicable technology to remove highly toxic and mobile chromate oxyanions from polluted water sources [1–5]. Large research efforts have been devoted to demonstrate the efficiency, low cost, and easy implementation of different photocatalysts to reduce hexavalent chromium to trivalent less mobile and toxic species [6–8]. Nevertheless, the scientific community has paid less attention to assess whether the photocatalysts are able to immobilize or adsorb the trivalent chromium cations [9] at the time that hexavalent species are photoreduced [10,11].

When approaching water remediation from a circular economy point of view, the conjunction of photocatalysis and adsorption functionalities in the same material is of paramount importance. For instance, at acidic conditions, trivalent chromium ions are still soluble in solution, and henceforth, they do not precipitate as chromium hydroxides/oxides after the photocatalytic reduction of Cr^{VI} [12]. At these acidic solutions, an additional immobilization step is necessary to extract Cr^{III} ions from the aqueous media. Here, the importance of bifunctional photocatalysts that are able to transform and retain chromium species is revealed, since they open the possibility to couple environmental remediation (photocatalysis) to chromium recovery (adsorption) [13]. It is important to note that chromium is currently located at the borderline of the European raw materials map because of its economic importance [14,15]. Indeed, the circular water remediation concept gains even more relevance if it is applied in highly concentrated and acidic water effluents from industrial (e.g., plating, alloying, tanning, textile dyes, pigments ...) and mining activities (e.g., acidic water streams) [16], since chromium recovery from these media becomes economically appealing [17]. The problem with acid rising waters derived from industrial platting or tanning activities is even more challenging than the revalorization of exhausted baths. In this case, chromium is highly diluted in large volumes of water, and its recovery by the usual technologies applied to concentrated exhausted electrolytic solutions (e.g., as liquid–liquid extraction, ion exchange and/or electrochemical separation [18] or precipitation, acid leaching, and subsequent precipitation [19,20]) is neither efficient nor economically appealing to revalorize the chromium ions. Diluted hexavalent chromium solutions require high-cost chemicals for its reduction to Cr^{III} until the legal maximum concentration limits for Cr^{VI} (ground water = 0.1 ppm, drinking water = 0.05 ppms) are accomplished. This scenario is where bifunctional photocatalyst sorbents could play a key role to face at the same time the water treatment coupled with the chromium recovery.

At the materials design level, a bifunctional photocatalyst applied for chromium recovery needs to be specifically tailored to (i) capture light and transform it to hole–electron pairs able to generate reactive oxygen radicals, and at the same time, (ii) to adsorb the chemical species transformed during photocatalysis. Therefore, efficient light harvesting [21], semiconducting nature [22], porosity [23–25], and chemical affinity to capture the transformed species are some of the key characteristics that need to be specifically encoded within the desired bifunctional catalyst [25]. Classic metal–oxide photocatalysts exhibit excellent photodegradation activities over a variety of pollutants, but their capacity to adsorb or retain the photodegradation intermediates and products is limited by its reduced porosity and surface areas [26–29]. In this context, metal–organic frameworks (MOFs) stand out as highly porous materials that are able to meet photoactivity and porosity. MOFs can be formed from semiconductor metal–oxide clusters and efficient light-harvesting organic linkers assembled in extended and ordered porous structures [27,30]. The combination of these two characteristics, together with the possibility to further decorate or engineer their structures, both pre and post synthetically, make MOFs the ideal candidates to combine photoreduction and adsorption properties [21,31–33].

Indeed, MOFs have been widely applied for chromium adsorption, photoreduction, and detection purposes, but their combined capacity to photoreduce and at the same time adsorb the phototransformed trivalent chromium ions has been rarely explored [34]. For instance, the photocatalytic activity of UiO-66-NH_2 and MIL-125 to transform Cr^{VI} to Cr^{III} has been proved under varied experimental conditions (e.g., chromate concentration,

photocatalyst loading, source of illumination, pH of the media, presence of competitor species...). In addition, our previous study points out that UiO-66-NH_2 is able to sorb quite efficiently both hexavalent and trivalent species from solution, exhibiting also a moderate capacity to chemically reduce the Cr^{VI} to Cr^{III} under dark conditions [35,36]. For instance, the chromium speciation within the Zr-MOF sorbents and photocatalysts has been successfully determined in our previous research by applying a multiple UV-Vis and electron paramagnetic resonance spectroscopy technique. Our findings confirmed that Cr^{VI} to Cr^{III} chemical and photoreduction processes are driven by the intermediate generation of pentavalent chromium transient species inside UiO-66-based materials [37] Nevertheless, this research does not unravel the fate of trivalent chromium phototransformed species in solution. This experimental gap—that is, the monitoring of both hexavalent and trivalent chromium in solution during working conditions—is common for most of the investigations carried out in Cr^{VI} to Cr^{III} photoreduction experiments. Most typically, during the MOF photocatalysis process, the concentration of the hexavalent chromium is experimentally determined by UV-Vis, overriding the monitoring of the trivalent chromium ions that could be still present after the photoreduction. In this work, we have fulfilled this gap, researching whether the photoactive MOFs can also act as efficient sorbents of the photoreduced species. The photoreduction and adsorptive capacities of two iconic photoactive water-stable zirconium and titanium-based MOFs, UiO-66 and MIL-125, have been addressed. For both materials, the experimental monitoring of Cr^{VI} and Cr^{III} in solution during and after the operation has been determined. Going a step forward, photoactive chromatographic columns based on UiO-66-NH_2 have been assembled to perform Cr^{VI} adsorption in a continuous flux mode. Our conclusions clearly point out that the studied bifunctional MOFs are able to completely photoreduce Cr^{VI} to Cr^{III} and at the same time immobilize reduce Cr^{III} species.

2. Results and Discussion

2.1. Metal-Organic Frameworks Selection, Synthesis, and Characterization

Among the varied MOFs that could potentially exhibit bifunctional photocatalytic and adsorption activities, zirconium amino-terephthalate (UiO-66-NH_2) and titanium terephthalate (MIL-125) compounds have been selected. Both MOFs exhibit a cubic structure with an "fcu" topology arising from the connectivity between the inorganic hexanuclear clusters through twelve terephthalate type organic linkers [38,39].

Further, the effect on the photocatalytic and adsorptive properties of (i) the particle size of MIL-125 material and (ii) the organic linker defect density of UiO-66-NH_2 have been studied. MIL-125 has been synthesized as micron-size particles applying hydrothermal synthesis (here and after denoted as MIL-125-H) and as nanoparticles (100–400 nm) under reflux conditions (here and after identified as MIL-125-R). Despite the bulk to surface proton coupled transfer in MIL-125 having been confirmed as highly independent of the particle size [30], it has been observed that the Cr^{VI} to Cr^{III} photoreduction kinetics are greatly affected by this parameter. In parallel, the density of organic linker defects in UiO-66-NH_2 materials has been modulated by the addition of hydrochloric acid to the reaction media. The addition of acid modulators to the synthesis media of Zr-based UiO-66-NH_2 generates a random displacement of amino-terephthalate organic linkers along its "fcu" crystal structure [31,40,41]. Two are the side effects of increasing the density of linker defects on the UiO-66-NH_2 properties: first, an increase of the overall surface area and pore volume, and second, the generation of preferential chemisorption positions for inorganic oxyanions [42–44]. Therefore, "defect-free" UiO-66-NH_2 and linker defective UiO-66-NH_2-def materials were synthesized at the same hydrothermal conditions but adding a controlled volume of HCl in the specific case of the defective sample.

Once synthesized, the quality, particle size, porosity, and optical properties of the materials were fully characterized by X-ray diffraction, UV-Vis spectroscopy, thermogravimetric analysis, transmission electron microscopy, and surface area measurements.

The X-ray diffraction (XRD) patterns of the synthesized samples are fully consistent with the simulated patterns obtained from UiO-66 and MIL-125 [38] structural models,

as can be observed in Figure 1a. Profile pattern analyses (Figure S1) confirm that there are no meaningful displacements of the cell parameters due to the generation of linker defects in UiO-66-NH_2-def, neither of which are associated to the particle size reduction from MIL-125-H to MIL-125-R (Table S1). XRD patterns show a significant increase of the peak width in the specific case of the samples with smaller particle size, which is ascribed to the reduction of the crystalline domains as a consequence of the synthesis conditions. This experimental evidence is confirmed by the micrographs obtained by means of transmission electron microscopy, as shown in Figure 1d. Indeed, for zirconium amino-terephthalate compounds, the addition of the HCl inorganic modulator induces an increase of the crystal size from 10–20 nm in non-defective UiO-66-NH_2 to 50–100 nm in UiO-66-NH_2 defective samples. A similar particle size dependence on the reaction temperature is found for titanium amino-terephthalate compounds. MIL-125-H, which was synthesized at 150 °C under hydrothermal conditions, exhibits a micron-size particle, whilst MIL-125-R, which was obtained from reflux conditions, crystallizes as spherical particles with diameters ranging from 100 to 400 nm. The light-harvesting capacity of the materials was studied by means of solid UV-Vis spectroscopy (Figure 1b). The results show that UiO-66 and MIL-125 materials present a very different behavior: while UiO-66 adsorbs in the visible range, the MIL-125 materials adsorb in the UV. UV-Vis spectra of UiO-66-NH_2 samples exhibit two main absorption bands ascribed to the visible light absorption by the amino-terephthalic organic linkers and UV-light harvesting driven by the zirconium inorganic clusters, respectively. As expected, the presence of linker defects in UiO-66-NH_2-def induces a blue shift displacement of the absorption band associated with the amino-terephthalate building units (UiO-66-NH_2 = 2.76 eV, UiO-66-NH_2-def = 2.82 eV). The different synthesis conditions (from MIL-125-H to MIL-125-R) induce a slight red shift to the charge-transfer absorption band associated to the titanium oxo-nuclear clusters.

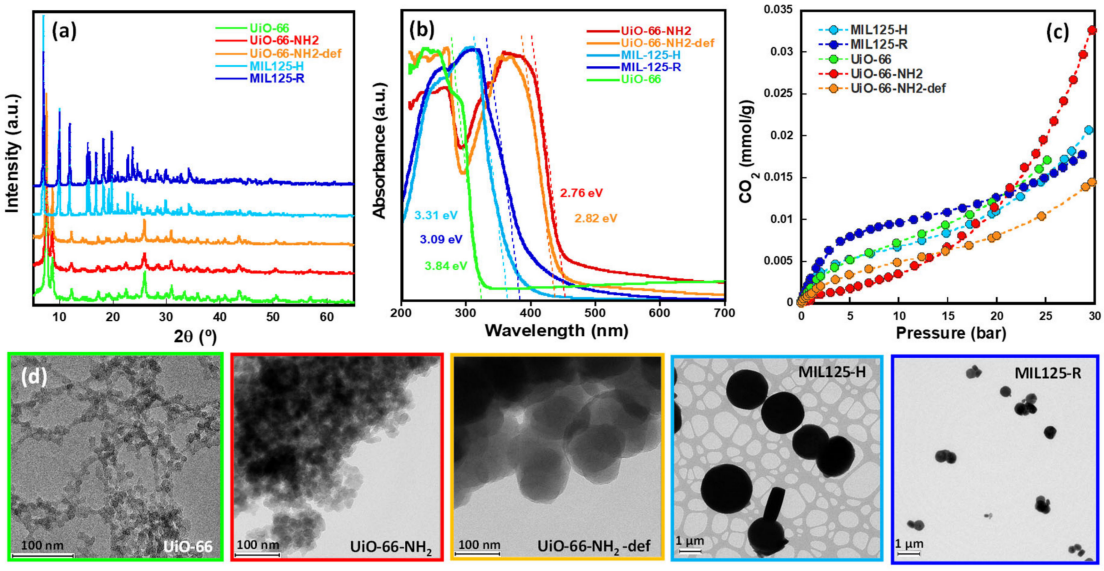

Figure 1. Characterization of the metal–organic frameworks (MOF) samples: (**a**) XRD patterns, (**b**) UV-Vis spectra, (**c**) CO_2 adsorption isotherms, and (**d**) TEM images.

The surface area and pore size distribution were determined from CO_2 adsorption isotherms at 273 K (Figure 1c). The Brunauer–Emmett–Teller (BET) surface area was calculated from the fitting of the linearized form of the BET equation (Figure S4). The obtained surface areas and microporous distribution (UiO-66 = 906 m^2/g, UiO-66-NH_2 = 894 m^2/g, UiO-66-NH_2-def = 600 m^2/g, MIL-125-H = 872 m^2/g, MIL-125-R = 1346 m^2/g) are in good agreement with previous reports [45,46]. The thermogravimetric analyses shown in Figure S2 allow quantifying the linker defect degree of UiO-66 materials applying

the protocol previously described by Shearer et al. [40]. TGA curves of UiO-66-NH_2 compounds show three main weight step losses ascribed to the release of the solvent entrapped within the pores (RT-100 °C), hydroxyl and water species coordinated to the inorganic clusters (150–350 °C), and calcination of the amino-terephthalate organic linkers (350–450 °C). The linker defect degree of UiO-66 samples can be estimated based on the weight loss percentage associated with the organic linker (see SI, Figure S3 and Table S2, for more detailed information). In the specific case of the UiO-66-NH_2 and UiO-66-NH_2-def synthesized in this work, 0.6 and 2.2 positions over the twelve carboxyl groups per inorganic clusters present in the ideal structure are vacant. The thermogravimetric analysis curves of MIL-125-H and MIL-125-R compounds show two main weight loss processes associated to (i) the release of water molecules entrapped within the pores (RT-100 °C) and (ii) the calcination of the amino-terephthalate linkers (350–480 °C).

According to that initial characterization, there would be an expected improved photoreduction efficiency for the samples with lower particle size as a result of the shorter migration path to the surface of the electron–hole pairs, which will lead to a more efficient generation of the reactive species that trigger the photoreduction. However, other parameters need to be considered in parallel. The light-harvesting capacity is also a key indicator of the photocatalytic efficiency dependence on the radiation wavelength (e.g., UVA, visible . . .) of our materials. Finally, linker functionalities of MOFs, such as amine groups, also favor the electron transfer along the framework while improving the chromium adsorption capacity.

2.2. Adsorption Kinetics of Cr^{VI} and Cr^{III} Ions

First, the adsorption affinity of UiO-66-NH_2 and MIL-125 samples over Cr^{VI} and Cr^{III} species was assessed by the evaluation of their adsorption kinetics over Cr^{VI} and Cr^{III} solutions at acidic conditions (pH = 3.5) (Figure 2). As expected from previous works, Zr-based UiO-66-NH_2 materials show fast kinetics and efficiencies over 90% to sorb both hexavalent and trivalent chromium species. For hexavalent chromium, the equilibrium is reached within the first 15 min of the experiment. In agreement with previous works [37], linker defective UiO-66-NH_2-def shows higher chromate adsorption capacity than the non-defective UiO-66-NH_2 (Figure 2a). It is well established that linker defective positions in Zr-based MOFs act as preferential adsorption points for anionic inorganic and organic species. For instance, hexavalent chromium is stabilized in a wide range of pH values as dichromate or hydrogen dichromate oxyanions [8,47]. On the contrary, MIL-125 materials show a negligible adsorption affinity over negative chromate anions, as expected because of the lack of defective linker positions of titanium terephthalate framework (Figure 2a).

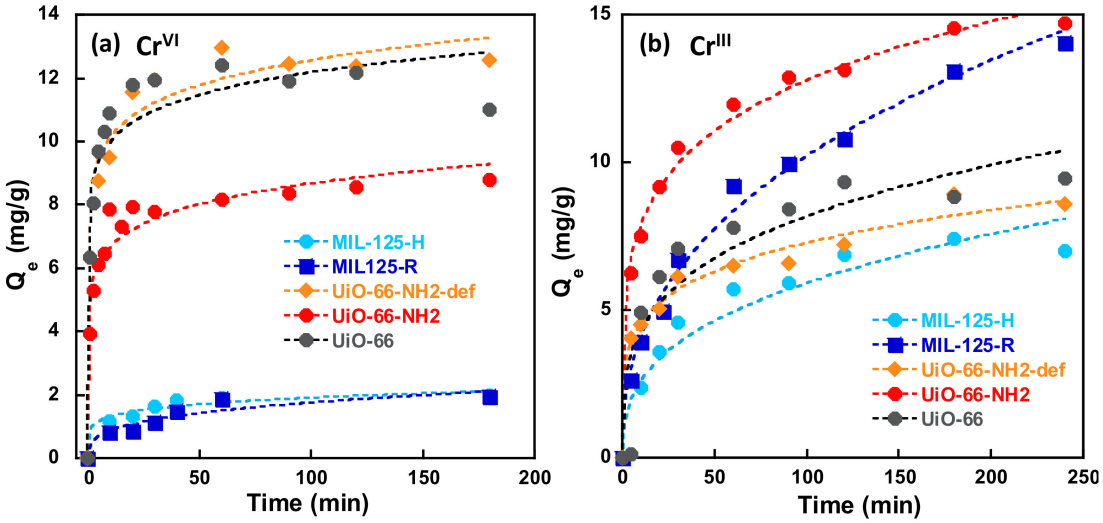

Figure 2. (**a**) Cr^{VI} and (**b**) Cr^{III} adsorption kinetics for UiO-66-NH_2 and MIL-125 samples. Points: experimental data. Line: Bangham model fitting. Adsorbent concentration 0.25 mg·mL^{-1}, C_i = 5 ppm.

Zr-UiO-66-NH_2 and MIL-125 compounds also exhibit adsorption over trivalent chromium, with adsorption capacities ranging from 8 to 15 mg/g for a 5 ppm solution. It is also worthwhile to notice the great impact that the particle size reduction has on the Cr^{III} adsorption capacity of MIL-125 type materials, since nano-sized MIL-125-R overperform the adsorbing capacity of its micron-size MIL-125-H homologue. Opposite, linker defective UiO-66-NH_2-def materials have larger particles size than that of the non-defective homologue, but their Cr^{VI} absorption capacity overperforms that of the UiO-66-NH_2 materials. In this case, the Cr^{VI} adsorption process is driven by the inner linker defects density instead by surface defects induced by the particle size reduction. In comparison to hexavalent chromate, Cr^{III} adsorption kinetics are slower, with equilibrium times above one hour. The time dependence of Cr^{VI} and Cr^{III} adsorption is well fitted by Bangham and pseudo-second order models (Figure 2b and Figure S5), while the pseudo-first-order model fails to reproduce the tendency above 60 min of adsorption, indicating that Cr^{VI} and Cr^{III} immobilization is not solely governed by diffusion processes, but also by chemisorption and/or chemical Cr^{VI} to Cr^{III} reduction processes into the MOF structure. Indeed, both the obtained adsorption capacity ($1/q_e$ for a pseudo-second-order model and m for Bangham's model) and kinetic rates ($1/V_0$ for pseudo-second-order model and K_T for Bangham's model) obtained from both models agree with the previous discussion regarding the adsorption capacity and affinity over Cr^{VI} and Cr^{III} species of the studied materials. The parameters obtained from the experimental fittings are summarized in Table 1 and allow quantifying the adsorption capacity and affinity of the studied materials over the main chromium species that will be involved in the photocatalysis experiments. As could be observed, some of the results are better fit by the Bangham model and others are better fit by the pseudo-second order model as a result of their different behavior toward chromium adsorption.

Table 1. Parameters obtained from the fitting of the Cr^{VI} and Cr^{III} adsorption kinetics shown in Figure 2 by applying the Bangham and pseudo-second-order models.

		Bangham's Model ($q_t = K_T \cdot t^{1/m}$)			**Pseudo-Second-Order Model ($t/qt = (1/V_0) + ((1/q_e) \cdot t)$)**		
	Ion	**R**	**K_T**	**M**	**R**	**$1/V_0$**	**$1/q_e$**
UiO-66	Cr^{VI}	0.9581	8.2 (6)	11 (2)	0.9982	−0.06 (9)	0.088 (2)
UiO-66-NH_2		0.9713	4.8 (2)	8.0 (8)	0.9997	0.29 (6)	0.1137 (9)
UiO-66-NH_2-def		0.9863	8.1 (6)	11 (2)	0.9997	0.16 (6)	0.0786 (7)
MIL-125-H		0.9799	0.88 (14)	6 (1)	0.99848	2.7 (9)	0.49 (1)
MIL-125-R		0.9559	0.43 (13)	3.3 (7)	0.98667	7 (2)	0.47 (3)
UiO-66	Cr^{III}	0.9193	2.3 (7)	3.6 (9)	0.9986	1.2 (3)	0.103 (2)
UiO-66-NH_2		0.9956	4.8 (3)	4.8 (3)	0.9987	0.9 (1)	0.065 (1)
UiO-66-NH_2-def		0.9897	2.8 (2)	4.9 (4)	0.9916	1.8 (6)	0.111 (5)
MIL-125-H		0.9517	1.2 (3)	2.8 (5)	0.9944	2.2 (6)	0.131 (5)
MIL-125-R		0.99512	1.63 (16)	2.5 (1)	0.99165	2.8 (4)	0.070 (3)

2.3. UiO-66-NH_2 Chromatographic Columns: Continuous Flux Adsorption

When designing continuous flux adsorption experiment, it is necessary to integrate the MOF in a highly permeable chromatographic column that at the same time maximizes the contact between the aqueous solution and the active MOF sorbent. First, the protocol described by Rapti et al. [48] was followed to assemble a UiO-66-NH_2/sand (1% *w*/*w*) based chromatographic column. Its adsorptive capacity was over Cr^{VI}. Results are shown in Figure 3.

The breakthrough adsorption experiment was carried out in dark conditions, with an initial Cr^{VI} concentration of 2.5 ppm and a 1 mL/min flux (Figure 3a). Experimental data for the adsorption stage in the open system was fitted to Thomas and Yoon-Nelson models, but results were not correctly fitted by these models [49].

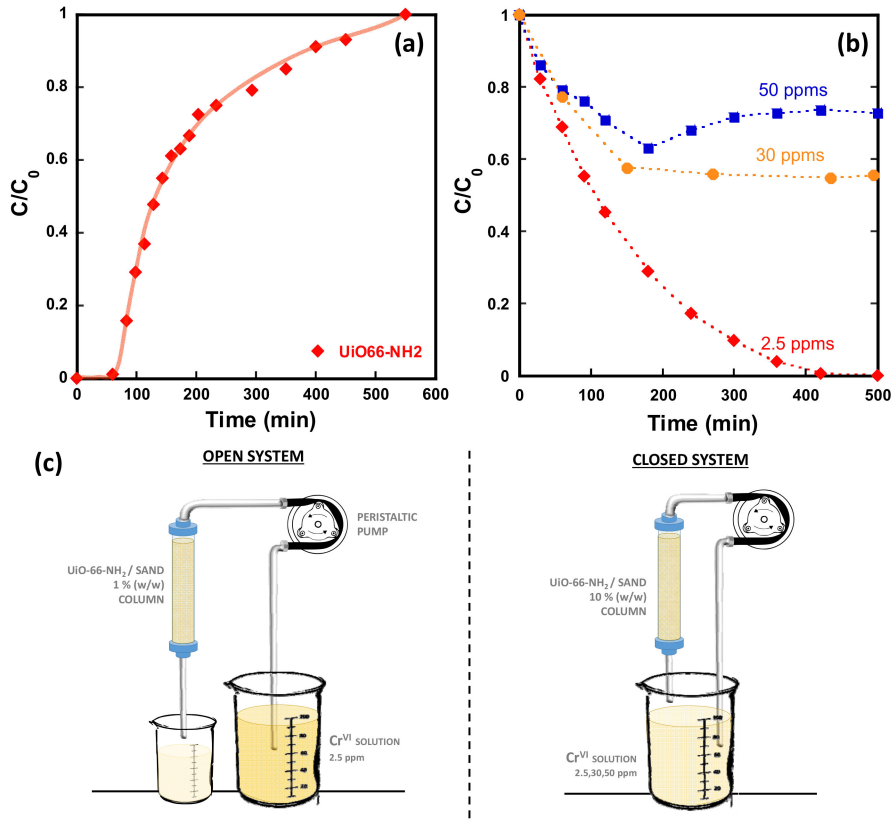

Figure 3. Continuous flux Cr^{VI} adsorption and photodegradation with UiO-66-NH_2 chromatographic columns. (**a**) Open circuit adsorption. 1% *w*/*w* UiO-66-NH_2/Sand column, [Cr^{VI}]= 2.5 ppm, Flux = 1 mL/min. (**b**) Closed circuit adsorption. 10% *w*/*w* UiO-66-NH_2/Sand column, [Cr^{VI}] = 2.5, 30 and 50 ppm, Flux= 1 mL/min. (**c**) Schematic representation of the open and closed circuits. Dashed lines are a guide to the eyes.

It is important to point out that the kinetics of adsorption differ significantly in static and continuous flux experiments. Indeed, in static mode, most of the Cr^{VI} adsorption occurs within the five initial minutes, while in continuous adsorption experiments, the sorbent saturation point is reached after 10 h.

Afterwards, we decided to increase the MOF content on the chromatographic column and evaluate its performance under a continuous flux process in a closed loop (see Figure S6 for a detailed information). By applying this strategy, the cumulative effect of the adsorption process in the long-term can be experimentally observed. Henceforth, 10% *w*/*w* UiO-66-NH_2/sand chromatographic columns were prepared, and 100 mL Cr^{VI} solutions of 2.5, 30, and 50 ppm concentrations were pumped at 1 mL/min flux until the adsorption equilibrium was reached. For the experiment performed with a 2.5 ppm concentration, the column was able to adsorb all the Cr^{VI} content in the 100 mL pumped across the column in 400 min. In the specific case of highly concentrated 50 ppm solution, the UiO-66-NH_2/sand column was able to retain almost 40% of the initial chromium in the adsorption stage. Indeed, a slight increase of the chromium content in the solution was observed after the saturation stage of the material. It is important to point that the color of the column changes appreciably during the experiments, suggesting that the material possess certain degree to induce a chemical reduction of Cr^{VI} to Cr^{III}. Finally, for the experiment performed at an intermediate concentration (Cr^{VI} = 30 ppms), the system was able to capture near 50% under dark conditions. It is clear that the time to reach the adsorption saturation stage is four-fold longer in the continuous flux conditions than in static adsorption experiments. It is interesting to note that the maximum adsorption capacities for the UiO-66-NH_2 material obtained from static sand adsorption experiments are very close. Indeed, 27 mg/g for static experiments, and 27 and 29 mg/g for continuous flux experiments were developed with 30 and 50 ppm solutions. Therefore, just by applying a

continuous flux adsorption experiment with column containing 1 g of UiO-66-NH_2, 12 L of water with 2.5 Cr^{VI} ppm concentration could be depolluted in a closed system.

2.4. Bifunctional Photocatalytic Reduction of Cr^{VI} to Cr^{III} and Coupled Adsorption of Cr^{III} Ions

Once the capacity of the different MOFs to adsorb Cr^{III} and Cr^{VI} species has been assessed, their Cr^{VI} to Cr^{III} photocatalytic reduction capacity was investigated. Thus, photoreduction curves were first measured under UVA light in a 5 ppm Cr^{VI} solution and at a sorbent loading of 0.25 g/L (Figure 4). A first adsorption stage in dark reveals that UiO-66-NH_2 type materials are able to capture more efficiently Cr^{VI} ions than the MIL-125 family, which is in good agreement with the Cr^{VI} adsorption kinetics presented above.

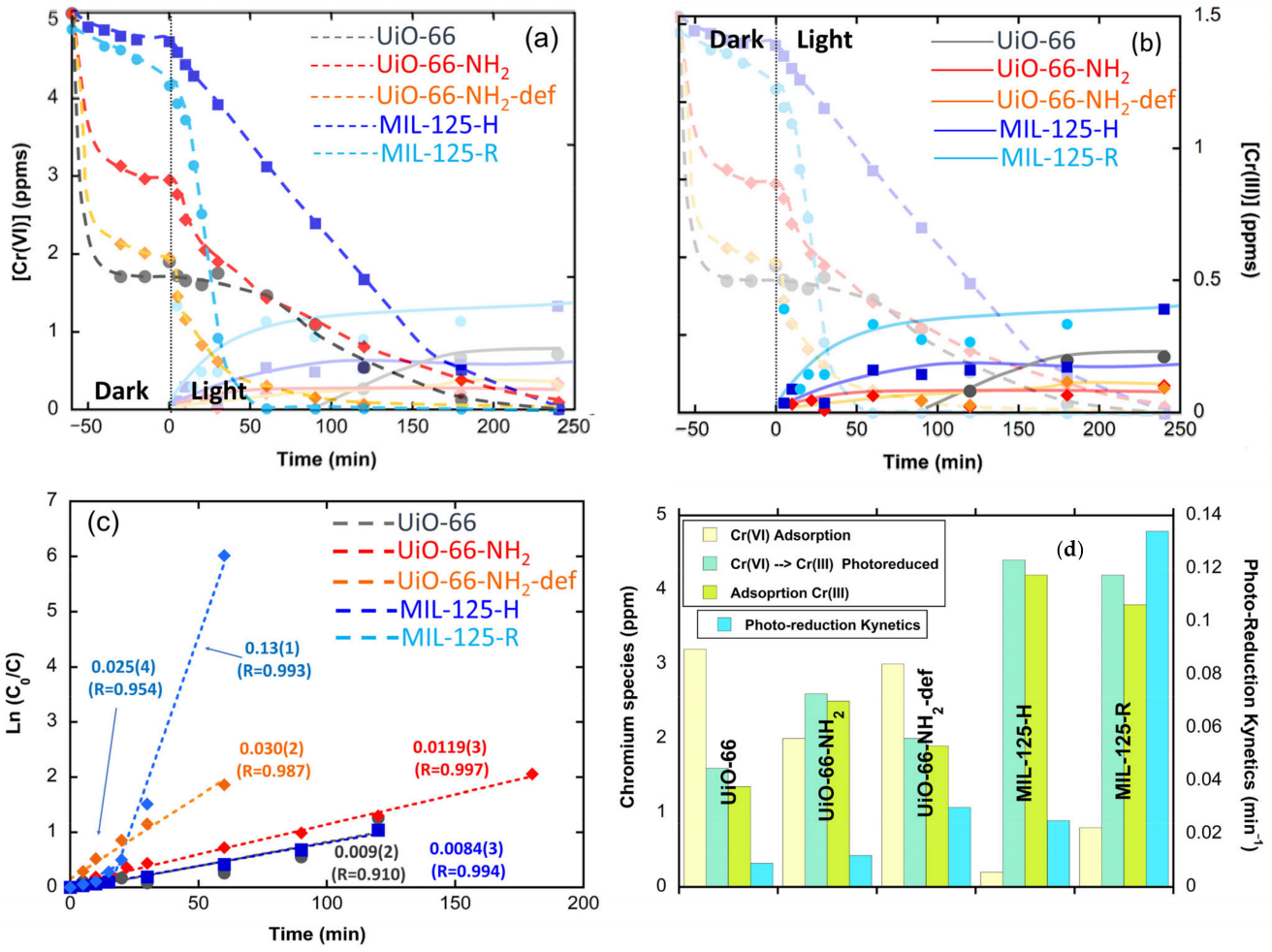

Figure 4. (**a**,**b**) Adsorption and photocatalytic reduction of Cr^{VI} in the different MOF samples under UVA light: (**a**) Detail of the Cr^{VI} and (**b**) Cr^{III} concentration evolutions. (**c**) Fitting of the photoreduction kinetics. (**d**) Summary of Cr^{VI} adsorbed at the MOF at dark conditions, the total amount of Cr^{VI} photoreduced to Cr^{III}, the amount of photoreduced Cr^{III} adsorbed at the MOF, and the photoreduction rate of the studied materials.

Nonetheless, a different trend is observed upon illumination, where MIL-125-R exhibits the most efficient photoreduction response and a kinetic rate compared to UiO-66 materials (Figure 4c,d), which can be related with its adsorption in the UVA range. On the contrary, the photoreduction capacity of MIL-125-H is appreciably slower. Even if the light-harvesting capacity is quite similar for both MIL125-R and MIL-125-H samples (Figure 1b), the shorter migration path to the surface of the electron–hole pairs in MIL-125-R nanoparticles with respect to the bigger ones for the MIL-125-H decreases their recombination,

and consequently, enhances the generation of the reactive species that trigger the photoreduction process (Figure 4).

In addition to the good photoreduction kinetics of MIL-125 materials, they also exhibit Cr^{III} adsorption capacity. The Cr^{III} concentration after the photoreduction process with MIL-125-R and MIL-125-H is quite low (<0.5 ppm), but it is still higher than the observed for UiO66-NH_2 materials (<0.1 ppm). Thus, in terms of photoreduction capacity plus Cr^{III} recovery, UiO-66 materials show the best combined performance. In addition to a high Cr^{VI} initial adsorption capacity, amino functionalized UiO-66 materials exhibit interesting kinetics for Cr^{VI} to Cr^{III} photoreduction, combined with a negligible loss of the generated Cr^{III}, due to their high adsorption capacity toward this cationic species.

The conclusions drawn by the photocatalytic experiments open relevant questions to properly understand the underlying processes that governs the photocatalytic and adsorptive dual function of the studied materials. In particular, it is important to address how the materials work under visible light illumination with the aim of evaluating their possible performance under solar light, as well as determining how the initial Cr^{VI} concentration just before the illumination stage affects the photoreduction kinetics.

In order to gain further insights regarding the above-mentioned issues, UiO-66-type materials have been selected because of their similarity in terms of crystal structure characteristics, allowing extracting meaningful conclusions from the experimental results. First, their photocatalytic capacity under visible light has been investigated. In order to enhance the photoreduction kinetics under visible light, the charge of the photocatalyst has been increased from the 0.25 g/L used in the previous experiments to 0.35 g/L. All the results are shown in Figure 5.

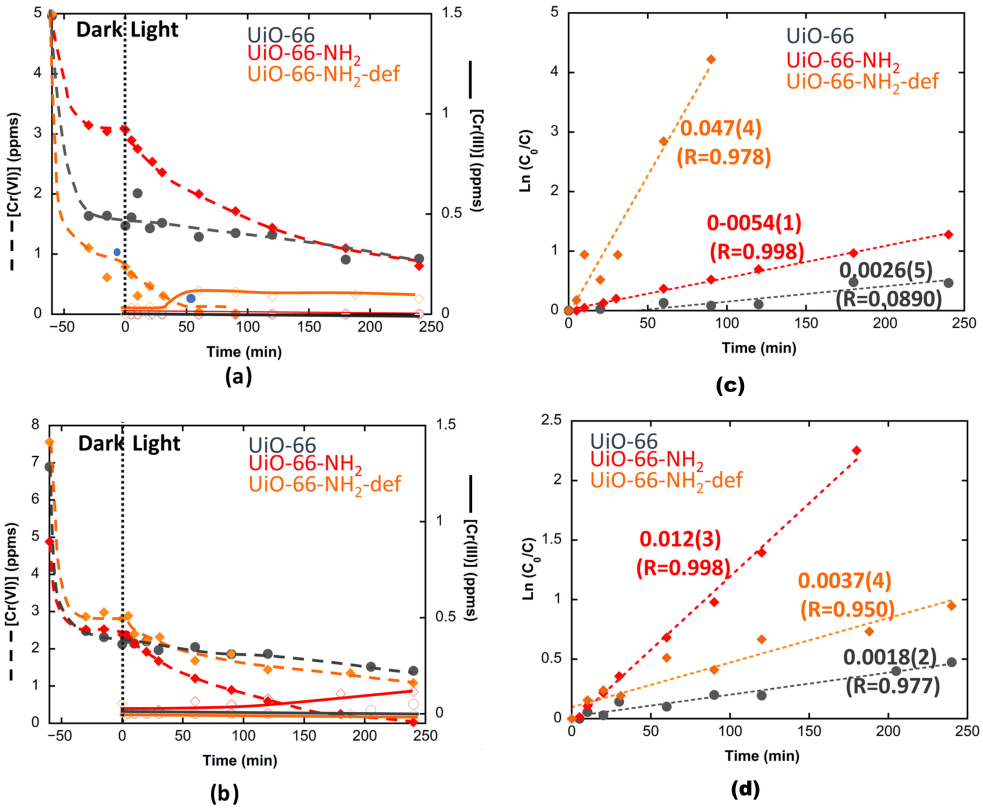

Figure 5. Adsorption and photocatalytic reduction of Cr^{VI} in the UiO-66 samples under visible light at a sorbent concentration of 0.35 g·L^{-1} starting (**a**) from the same initial concentration and (**b**) after modifying the initial concentration to reach the same Cr^{VI} content in the solution after finalizing the adsorption in dark conditions. (**c**,**d**) Fitting of the photoreduction kinetics.

The increase on the MOF's photocatalysts loading generates a higher Cr^{VI} retention in the dark, being the most efficient adsorbent of the UiO-66-NH_2-def material, followed by UiO-66 and UiO-66-NH_2. Regarding the photocatalytic process in visible light (Figure 5a), it is observed that amine functionalities play again an important role in the chromium photoreduction compared with UiO-66 non-functionalized samples as a result of their improved light harvesting (Figure 1b). Amino decorated UiO-66-NH_2 materials exhibit higher efficiencies and faster kinetics (Figure 5c) than UiO-66, achieving 100% (UiO-66-NH_2-def) and 60% (UiO-66-NH_2) photocatalytic efficiencies in about 1 h. This indicates the feasibility of applying these photocatalysts under solar irradiation. Regarding Cr^{III}, a small increase in the concentration of this species is observed in the solution during the photoreduction process, but it is still very low (≈0.1 ppm) when compared to the starting Cr^{VI} concentration.

Once it was confirmed that the photoactivity and adsorption-coupled capacity of UiO-66-NH_2 materials are still functional under visible light illumination, chromium photoreduction experiments were performed starting from a similar Cr^{VI} concentration before illumination (Figure 5b). To this end, the initial Cr^{VI} concentration was increased until a value close to 3 ppms was obtained after the initial adsorption stage. Thus, the photocatalytic kinetics were compared starting from similar conditions. As it could be observed in Figure 5b, when the photoreduction process starts from a similar initial concentration, the UiO-66-NH_2 photocatalyst presents improved photoreduction kinetics, which is followed by UiO-66-NH_2-def and UiO-66 materials. It is important to note that the calculated photocatalytic rates (Figure 5d) are quite different from those obtained from the previous experiments (Figure 5c), where the Cr^{VI} concentration after adsorption differs significantly for the three studied compounds. Indeed, generically speaking, the higher the Cr^{VI} concentration before the illumination stage, the lower the photocatalytic rate.

The photoreduction kinetic rates obtained from Figure 4b,d reveal that this parameter is affected by the particles size and by the light-harvesting capacity in the visible, as well as by the experimental conditions themselves. Independently of the experimental conditions, overall, the Cr^{III} adsorption efficiencies are above 98%, although a slight increment of the Cr^{III} concentration in solution has been observed under certain experimental conditions. Further investigations are needed to elucidate the activation and reusability of the studied materials, as well as the Cr^{III} saturation point under photocatalysis experiments.

3. Materials and Methods

3.1. Synthesis of Metal-Organic Framework Photocatalysts

UiO-66, UiO-66-NH_2, and UiO-66-NH_2-def were prepared through a slightly modified solvothermal synthesis previously reported [41,43]. First, zirconium chloride (Aldrich, San Luis, MO, USA) (0.5418 g) was dissolved in 60 mL of dimethylformamide (DMF, Aldrich, San Luis, MO, USA)) under stirring in a Pyrex® (Fisher Scientific, Waltham, MA, USA) autoclave. Afterwards, terephthalic (0.38012 g, BDC, Aldrich, San Luis, MO, USA) or amino terephthalic acid (0.4185 g, BDC-NH_2, Aldrich, San Luis, MO, USA) and distilled water (1.5 mL) were added to the zirconium chloride solution under continuous stirring in order to obtain the UiO-66 and UiO-66-NH_2 samples. UiO-66-NH_2-def sample synthesis requires the addition of 1 mL of HCl (37% *v/v,* Aldrich, San Luis, MO, USA) solution to the $ZrCl_4$ and amino terephthalic DMF mixture. Once a clear solution is obtained, the Pyrex® reactor was closed and placed in a preheated oven (80 °C for 24 h). After that, the sample was recovered by centrifugation and washed three times overnight with methanol. Finally, the compound was dried at 80 °C for 12 h. An MIL-125-H sample was prepared following the hydrothermal protocol previously established by Dan-Hardi et al. [38]. Reflux synthesis of MIL-125-R was developed applying a protocol adapted from ref [50]. First, 7.70 g of BDC was dissolved in 100 mL of DMF under reflux and continuous stirring at 100 °C for 1 h. Then, 28 mL of methanol (99.9 %, Aldrich, San Luis, MO, USA) was added to the solution and further stirred for 1 h. Afterwards, 8.4 mL of $Ti(iPrO)_4$ (97 %, Aldrich, San Luis, MO, USA) was added drop by drop to prevent the formation of agglomerates.

Samples were refluxed for three days, recovered, and thoroughly washed with DMF and ethanol to remove the non-reacted reagents.

3.2. Characterization Protocols

The MOF photocatalysts were fully characterized by means of XRD, CO_2 adsorption isotherms, electron transmission microscopy, and UV-Vis spectroscopy. The results show that the structural, textural, spectroscopic, optical, and thermal properties are in good agreement with previously reported studies. More detailed information about the characterization protocols can be found in the Supplementary Information.

3.3. Adsorption Kinetics

Cr^{VI} and Cr^{III} adsorption kinetics were conducted in the same conditions as those of the photoreduction experiments (5 ppm Cr^{VI} or Cr^{III} solution, 0.25 g/L of adsorbent) but in the absence of light. Then, 5 mL aliquots were taken from the solution at different time intervals until equilibrium. The quantification of Cr^{VI} was performed based on the previously reported diphenyl carbazide colorimetric methodology [51]. Cr^{III} estimation was achieved after oxidizing it to Cr^{VI} and applying the same colorimetric protocol. For that, 5 mL of the chromium solution, 100 µL of a 3.39M H_2SO_4 (98%, Aldrich, San Luis, MO, USA) solution, and 100 µL of a 22.6 mM solution were added. The mixture was heated at 100 °C for 20 min and then cooled down to room temperature in a water bath. Afterwards, 50 µL of a NaN_3 solution were added to the mixture until the purple color of the potassium permanganate disappears from the solution. Finally, diphenyl carbazide colorimetric methodology was used to quantify the chromium content. Results were fitted to Bangham and pseudo-first and second-order kinetic models [52]. A concentration of 5 ppm was chosen as a model of diluted raising water derived from the electrolytic bath cleaning. This concentration is slightly higher than that usually found in rives and underground waters polluted by the tanning or planting industry (1 to 0.5 ppms).

3.4. Photocatalytic Reduction of Cr^{VI} to Cr^{III}

Photocatalysis experiments were conducted in a 5 ppm Cr^{VI} solution using 0.25 g/L and under UVA and Vis light. First, 50 mg of the photocatalyst was immersed in 200 mL solution of Cr^{VI} 5 ppm solution under stirring in the dark. Once an adsorption equilibrium condition was achieved, 5 mL aliquots were taken at different times under illuminated conditions. Cr^{VI} and Cr^{III} quantification was carried out as previously described.

3.5. Continuous Flux Adsorption Experiments

Open chromatographic columns of 1% weight of UiO-66-NH_2 (0.0125 g) in sand (1.25 g) were assembled as illustrated in Figure S6. A continuous flux of 1 mL/min of a chromium solution of 2.5 ppm concentration was passed through the column, and the Cr^{VI} concentration was monitored during the process. Closed columns were assembled from a UiO-66-NH_2 (10% *w/w*, 0.125 g) diluted in 1.25 g of sand. Then, 100 mL of a 1 mL/min flux of 2.5, 30, and 50 ppm chromium solution was pumped through the column until the chromium concentration reaches a stable value, that is, the MOF has reached its saturation point.

4. Conclusions

The dual photocatalytic and adsorptive functionality of archetypal Zr and Ti-based metal–organic frameworks over the simultaneous Cr^{VI} to Cr^{III} photoreduction and Cr^{III} immobilization has been demonstrated. The particle size reduction of Ti-based MIL-125 has been revealed as a key parameter to enhance the photoactivity of the material, whilst the linker defective chemistry of Zr-based UiO-66 compounds is detrimental for the chromium photoreduction but beneficial for the retention of the Cr^{III} phototransformed species. Considered as a whole, the bifunctional Zr and Ti-based MOFs are able to retain from 90 to 98% of the initial chromium present at acidic solutions. A photodegradation

and adsorption coupled process can be performed efficiently on a continuous flux closed loop circuit when the MOF active material is assembled as a chromatographic column. The experimental procedure described in this work opens the future perspective to test the bifunctional catalytic and adsorptive capacity of photoactive MOFs synthesized so far, not just applied for the specific case of chromium, but also for homologous studies such as the As^{III} to As^{V} arsenic photooxidation or emerging pollutant photodegradation coupled to the adsorption of the photogenerated intermediate products. However, it is important to note that further research is needed to consider in a quantitative manner the economic and technical feasibility of MOFs for chromium recovery in real scenarios far from ideal laboratory models. Many questions are raised from the current work, such as (1) to which extend the MOF chemistry is applicable far from diluted rising industrial waters, that is, in high concentration industrial solutions as exhausted metal acidic baths, (2) or at intermediate slightly acidic solutions obtained after the neutralization of the initial bath electrolytes. (3) Can the chromium recovery from the MOF system leading to Cr^{III} solution of 20 g/L concentration be reused in plating electrolyte media? Furthermore, could the process be performed in a repetitive way without damaging the framework and properties of our hybrid inorganic–organic systems?

Supplementary Materials: The following are available online at https://www.mdpi.com/2073-4344/11/1/51/s1, Description of Materials and processing methods, Characterization techniques and procedures, Performance assessment, DRX, TGA, and BET fittings (Figures S1–S5). Table S1: Cell parameters determined by XRD and Table S2: Calculated weight loss related to ligand calcination step of TGA analysis.

Author Contributions: Conceptualization, R.F.d.L. and A.G.; methodology, P.G.S., A.V., B.G.-N., M.R., A.R., Y.M.Q. formal analysis, P.G.S., A.V., B.G.-N., M.R., A.F.-M., J.O.; investigation, P.G.S., A.V., B.G.-N., M.R., E.S.L., Y.M.Q.; data curation, P.G.S., A.V., B.G.-N., M.R., A.F.-M., Y.M.Q.; writing—original draft preparation, P.G.S., A.V. and R.F.d.L.; writing—review and editing, R.F.d.L., A.G., S.L.-M., P.G.S., E.S.L.; visualization, P.G.S.; B.G-N., supervision, R.F.d.L. and A.G.; project administration, R.F.d.L., A.G., S.L.-M., M.I.A. and; funding acquisition, R.F.d.L., A.G., S.L.-M., M.I.A. All authors have read and agreed to the published version of the manuscript.

Funding: The authors thank the financial support from the Spanish Ministry of Economy and Competitiveness (MINECO) through projects MAT2016-76739-R (AEI/FEDER, EU) and MAT2016-76039-C4-3-R (AEI/FEDER, UE) (including FEDER financial support) and from the Basque Government Industry and Education Departments under the ELKARTEK (LION, ACTIMAT), HAZITEK (SIMAN) and PIBA (PIBA-2018-06) programs, respectively. The European Commission Research & Innovation H2020-MSCA-RISE-2017 (Ref.: 778412) INDESMOF project.

Institutional Review Board Statement: Not applicable.

Informed Consent Statement: Not applicable.

Data Availability Statement: Data available on request due to restrictions. The data presented in this study are available on request from the corresponding author. The data are not publicly available due to possible future exploitation actions of the results presented in this study.

Acknowledgments: The authors also thank for technical and human support provided by SGIker (UPV/EHU/ERDF, EU).

Conflicts of Interest: The authors declare no conflict of interest.

References

1. Dimitrova, D.G. Iron Based Metal Organic Frameworks as Photocatalysts for Chromium (VI) Degradation. Bachelor's Thesis, University College Utrecht, Utrecht, The Netherlands, 2015.
2. Bedia, J.; Muelas-ramos, V.; Peñas-garzón, M.; Gómez-avilés, A.; Rodríguez, J.J.; Belver, C. A review of photocatalytic water purification with metal organic frameworks. *Catalysts* **2019**, *9*, 52. [CrossRef]
3. Yuan, S.; Qin, J.S.; Lollar, C.T.; Zhou, H.C. Stable Metal-Organic Frameworks with Group 4 Metals: Current Status and Trends. *ACS Cent. Sci.* **2018**, *4*, 440–450. [CrossRef] [PubMed]
4. Assi, H.; Mouchaham, G.; Steunou, N.; Devic, T.; Serre, C. Titanium coordination compounds: From discrete metal complexes to metal-organic frameworks. *Chem. Soc. Rev.* **2017**, *46*, 3431–3452. [CrossRef] [PubMed]

5. Zhao, S.; Wang, G.; Poelman, D. Metal Organic Frameworks Based Materials for Heterogeneous Photocatalysis. *Molecules* **2018**, *2*, 2947. [CrossRef] [PubMed]
6. Daier, V.; Signorella, S.; Rizzotto, M.; Frascaroli, M.I.; Palopoli, C.; Brondino, C.; Salas-Peregrin, J.M.; Sala, L.F. Kinetics and mechanism of the reduction of cr(VI) to cr(III) by D-ribose and 2-deoxy-D-ribose. *Can. J. Chem.* **1999**, *77*, 57–64. [CrossRef]
7. Azimi, A.; Azari, A.; Rezakazemi, M.; Ansarpour, M. Removal of Heavy Metals from Industrial Wastewaters: A Review. *ChemBioEng Rev.* **2017**, *4*, 37–59. [CrossRef]
8. Unceta, N.; Séby, F.; Malherbe, J.; Donard, O.F.X. Chromium speciation in solid matrices and regulation: A review. *Anal. Bioanal. Chem.* **2010**, *397*, 1097–1111. [CrossRef]
9. Reizabal, A.; Costa, C.M.; Saiz, P.G.; Gonzalez, B.; Pérez-Álvarez, L.; Fernández de Luis, R.; Garcia, A.; Vilas-Vilela, J.L.; Lanceros-Méndez, S. Processing Strategies to Obtain Highly Porous Silk Fibroin Structures with Tailored Microstructure and Molecular Characteristics and Their Applicability in Water Remediation. *J. Hazard. Mater.* **2020**, *403*, 123675. [CrossRef]
10. Matos, J.; Rosales, M.; García, A.; Nieto-Delgado, C.; Rangel-Mendez, J.R. Hybrid photoactive materials from municipal sewage sludge for the photocatalytic degradation of methylene blue. *Green Chem.* **2011**, *13*, 3431–3439. [CrossRef]
11. Rosales, M.; Zoltan, T.; Yadarola, C.; Mosquera, E.; Gracia, F.; García, A. The influence of the morphology of 1D TiO 2 nanostructures on photogeneration of reactive oxygen species and enhanced photocatalytic activity. *J. Mol. Liq.* **2019**, *281*, 59–69. [CrossRef]
12. Valverde, A.; Gsaiz, P.; Orive, J.; Larrea, E.; Reizabal-Para, A.; Tovar, G.; Copello, G.; Lazaro-Martinez, J.M.; Rodriguez, B.; Gonzalez-Navarrete, B.; et al. Porous, lightweight, metal organic materials: Environment sustainability. In *Advanced Lightweight Multifunctional Materials*; Elsevier: Amsterdam, The Netherlands, 2020; pp. 43–130.
13. Maleki, A.; Hayati, B.; Naghizadeh, M.; Joo, S.W. Adsorption of hexavalent chromium by metal organic frameworks from aqueous solution. *J. Ind. Eng. Chem.* **2015**, *28*, 211–216. [CrossRef]
14. Massari, S.; Ruberti, M. Rare earth elements as critical raw materials: Focus on international markets and future strategies. *Resour. Policy* **2013**, *38*, 36–43. [CrossRef]
15. Wübbeke, J. Rare earth elements in China: Policies and narratives of reinventing an industry. *Resour. Policy* **2013**, *38*, 1–11. [CrossRef]
16. Martins, P.M.; Salazar, H.; Aoudjit, L.; Gonçalves, R.; Zioui, D.; Fidalgo-Marijuan, A.; Costa, C.M.; Ferdov, S.; Lanceros-Mendez, S. Crystal morphology control of synthetic giniite for enhanced photo-Fenton activity against the emerging pollutant metronidazole. *Chemosphere* **2020**, *262*, 128300. [CrossRef] [PubMed]
17. Torras, J.; Buj, I.; Rovira, M.; de Pablo, J. Chromium recovery from exhausted baths generated in plating processes and its reuse in the tanning industry. *J. Hazard. Mater.* **2012**, *209–210*, 343–347. [CrossRef] [PubMed]
18. de Souza e Silva, P.T.; de Mello, N.T.; Menezes Duarte, M.M.; Montenegro, M.C.B.S.M.; Araújo, A.N.; de Barros Neto, B.; da Silva, V.L. Extraction and recovery of chromium from electroplating sludge. *J. Hazard. Mater.* **2006**, *128*, 39–43. [CrossRef] [PubMed]
19. Gupta, B.; Deep, A.; Tandon, S.N. Recovery of Chromium and Nickel from Industrial Waste. *Ind. Eng. Chem. Res.* **2002**, *41*, 2948–2952. [CrossRef]
20. Chmielewski, A.G.; Urbański, T.S.; Migdał, W. Separation technologies for metals recovery from industrial wastes. *Hydrometallurgy* **1997**, *45*, 333–344. [CrossRef]
21. Karagiaridi, O.; Bury, W.; Mondloch, J.E.; Hupp, J.T.; Farha, O.K. Solvent-assisted linker exchange: An alternative to the de novo synthesis of unattainable metal-organic frameworks. *Angew. Chem. Int. Ed.* **2014**, *53*, 4530–4540. [CrossRef]
22. Khalil, L.B.; Mourad, W.E.; Rophael, M.W. Photocatalytic reduction of environmental pollutant Cr (VI) over some semiconductors under UV /visible light illumination. *Appl. Catal. B Environ.* **1998**, *17*, 267–273. [CrossRef]
23. Stassin, T.; Reinsch, H.; Van de Voorde, B.; Wuttke, S.; Medina, D.D.; Stock, N.; Bein, T.; Ameloot, R.; De Vos, D. Adsorption and Reactive Desorption on Metal–Organic Frameworks: A Direct Strategy for Lactic Acid Recovery. *ChemSusChem* **2017**, *10*, 643–650. [CrossRef] [PubMed]
24. Ji, Z.; Wang, H.; Canossa, S.; Wuttke, S.; Yaghi, O.M. Pore Chemistry of Metal–Organic Frameworks. *Adv. Funct. Mater.* **2020**, *30*, 2000238. [CrossRef]
25. Connolly, B.M.; Aragones-Anglada, M.; Gandara-Loe, J.; Danaf, N.A.; Lamb, D.C.; Mehta, J.P.; Vulpe, D.; Wuttke, S.; Silvestre-Albero, J.; Moghadam, P.Z.; et al. Tuning porosity in macroscopic monolithic metal-organic frameworks for exceptional natural gas storage. *Nat. Commun.* **2019**, *10*, 2345. [CrossRef] [PubMed]
26. Xu, S.C.; Pan, S.S.; Xu, Y.; Luo, Y.Y.; Zhang, Y.X.; Li, G.H. Efficient removal of Cr(VI) from wastewater under sunlight by Fe(II)-doped TiO2 spherical shell. *J. Hazard. Mater.* **2015**, *283*, 7–13. [CrossRef] [PubMed]
27. Feng, Y.; Chen, Q.; Cao, M.; Ling, N.; Yao, J. Defect-Tailoring and Titanium Substitution in Metal-Organic Framework UiO-66-NH2 for the Photocatalytic Degradation of Cr(VI) to Cr(III). *ACS Appl. Nano Mater.* **2019**, *2*, 5973–5980. [CrossRef]
28. Zhang, Y.; Xu, M.; Li, H.; Ge, H.; Bian, Z. The enhanced photoreduction of Cr(VI) to Cr(III) using carbon dots coupled TiO2 mesocrystals. *Appl. Catal. B Environ.* **2018**, *226*, 213–219. [CrossRef]
29. Costa, I.G.F.; Terra, N.M.; Cardoso, V.L.; Batista, F.R.X.; Reis, M.H.M. Photoreduction of chromium(VI) in microstructured ceramic hollow fibers impregnated with titanium dioxide and coated with green algae Chlorella vulgaris. *J. Hazard. Mater.* **2019**, *379*, 120837. [CrossRef]
30. Saouma, C.T.; Richard, S.; Smolders, S.; Delley, M.F.; Ameloot, R.; Vermoortele, F.; De Vos, D.E.; Mayer, J.M.; Saouma, C.T.; Richard, S.; et al. Bulk-to-Surface Proton-Coupled Electron Transfer Reactivity of the Metal–Organic Framework MIL-125. *J. Am. Chem. Soc.* **2018**. [CrossRef]

31. Muguruza, A.R.; de Luis, R.F.; Iglesias, N.; Bazán, B.; Urtiaga, M.K.; Larrea, E.S.; Fidalgo-Marijuan, A.; Barandika, G. Encapsulation of β-alanine model amino-acid in zirconium(IV) metal organic frameworks: Defect engineering to improve host guest interactions. *J. Inorg. Biochem.* **2020**, *205*, 110977. [CrossRef]
32. Ali Akbar Razavi, S.; Morsali, A. Linker functionalized metal-organic frameworks. *Coord. Chem. Rev.* **2019**, *399*, 213023. [CrossRef]
33. Huang, L.; He, M.; Chen, B.; Hu, B. A mercapto functionalized magnetic Zr-MOF by solvent-assisted ligand exchange for Hg2+ removal from water. *J. Mater. Chem. A* **2016**, *4*, 5159–5166. [CrossRef]
34. Wang, C.C.; Du, X.D.; Li, J.; Guo, X.X.; Wang, P.; Zhang, J. Photocatalytic Cr(VI) reduction in metal-organic frameworks: A mini-review. *Appl. Catal. B Environ.* **2016**, *193*, 198–216. [CrossRef]
35. Shen, L.; Liang, S.; Wu, W.; Liang, R.; Wu, L. Multifunctional NH2-mediated zirconium metal– organic framework as an efficient visible-light-driven photocatalyst for selective oxidation of alcohols and reduction of aqueous Cr(VI). *Dalt. Trans.* **2013**, *42*, 13649–13657. [CrossRef] [PubMed]
36. Wang, Z.; Yang, J.; Li, Y.; Zhuang, Q.; Gu, J. Simultaneous Degradation and Removal of CrVIfrom Aqueous Solution with Zr-Based Metal–Organic Frameworks Bearing Inherent Reductive Sites. *Chem. A Eur. J.* **2017**, *23*, 15415–15423. [CrossRef]
37. Saiz, P.G.; Iglesias, N.; Gonzalez-Navarrete, B.; Rosales, M.; Quintero, Y.M.; Reizabal, A.; Orive, J.; Fidalgo-Marijuan, A.; Lanceros-Mendez, S.; Arriortua, M.I.; et al. Chromium speciation in zirconium-based metal-organic frameworks for environmental remediation. *Chem. Eur. J.* **2020**, *26*, 1–13. [CrossRef]
38. Dan-hardi, M.; Serre, C. A new photoactive crystalline highly porous titanium (IV) dicarboxylate. *JACS* **2009**, *131*, 10857–10859. [CrossRef]
39. Cavka, J.H.; Jakobsen, S.; Olsbye, U.; Guillou, N.; Lamberti, C.; Bordiga, S.; Lillerud, K.P. A new zirconium inorganic building brick forming metal organic frameworks with exceptional stability. *J. Am. Chem. Soc.* **2008**, *130*, 13850–13851. [CrossRef]
40. Shearer, G.C.; Chavan, S.; Ethiraj, J.; Vitillo, J.G.; Svelle, S.; Olsbye, U.; Lamberti, C.; Bordiga, S.; Lillerud, K.P. Tuned to perfection: Ironing out the defects in metal-organic framework UiO-66. *Chem. Mater.* **2014**, *26*, 4068–4071. [CrossRef]
41. Øien, S.; Wragg, D.; Reinsch, H.; Svelle, S.; Bordiga, S.; Lamberti, C.; Lillerud, K.P. Detailed structure analysis of atomic positions and defects in Zirconium Metal—Organic Frameworks. *Cryst. Growth Des.* **2014**, *14*, 5370–5372. [CrossRef]
42. Audu CO Nguyen HG, T.; Chang, C.Y.; Katz, M.J.; Mao, L.; Farha, O.K.; Hupp, J.T.; Nguyen, S.T. The dual capture of AsV and AsIII by UiO-66 and analogues. *Chem. Sci.* **2016**, *7*, 6492–6498. [CrossRef]
43. Shearer, G.C.; Chavan, S.; Bordiga, S.; Svelle, S.; Olsbye, U.; Lillerud, K.P. Defect engineering: Tuning the porosity and composition of the metal−organic framework UiO-66 via modulated synthesis. *Chem. Mater.* **2016**, *28*, 3749–3761. [CrossRef]
44. Wang, C.; Liu, X.; Chen, J.P.; Li, K. Superior removal of arsenic from water with zirconium metal-organic framework UiO-66. *Sci. Rep.* **2015**, *5*, 1–10. [CrossRef] [PubMed]
45. Sohail, M.; Yun, Y.; Lee, E.; Kim, S.K.; Cho, K.; Kim, J.; Kim, T.W.; Moon, J.; Kim, H. Synthesis of Highly Crystalline NH 2—MIL-125 (Ti) with S—Shaped Water Isotherms for Adsorption Heat Transformation. *Cryst. Growth Des.* **2017**, *125*, 2–7. [CrossRef]
46. Chavan, S.M.; Shearer, G.C.; Svelle, S.; Olsbye, U.; Bonino, F.; Ethiraj, J.; Lillerud, K.P.; Bordiga, S. Synthesis and characterization of amine-functionalized mixed-ligand metal−organic frameworks of UiO-66 topology. *Inorg. Chem.* **2014**, *53*, 9509–9515. [CrossRef] [PubMed]
47. Rakhunde, R.; Deshpande, L.; Juneja, H.D. Chemical speciation of chromium in water: A review. *Crit. Rev. Environ. Sci. Technol.* **2012**, *42*, 776–810. [CrossRef]
48. Rapti, S.; Pournara, A.; Sarma, D.; Papadas, I.T.; Armatas, G.S.; Hassan, Y.S.; Alkordi, M.H.; Kanatzidis, M.G.; Manos, M.J. Rapid, green and inexpensive synthesis of high quality UiO-66 amino-functionalized materials with exceptional capability for removal of hexavalent chromium from industrial waste. *Inorg. Chem. Front.* **2016**, *3*, 635–644. [CrossRef]
49. Torres, D.I.; Lazaro-Martínez, J.M.; Copello, G.J.; dall Orto, V.C. Single step synthesis of a polyhydroxy ether and its optimization to adsorption of a textile dye. *J. Environ. Chem. Eng.* **2019**, 103416. [CrossRef]
50. Wang, H.; Yuan, X.; Wu, Y.; Zeng, G.; Chen, X.; Leng, L.; Wu, Z.; Jiang, L.; Li, H. Facile synthesis of amino-functionalized titanium metal-organic frameworks and their superior visible-light photocatalytic activity for Cr (VI) reduction. *J. Hazard. Mater.* **2015**, *286*, 187–194. [CrossRef]
51. Sereshti, H.; Vasheghani Farahani, M.; Baghdadi, M. Trace determination of chromium(VI) in environmental water samples using innovative thermally reduced graphene (TRG) modified SiO2 adsorbent for solid phase extraction and UV-vis spectrophotometry. *Talanta* **2016**, *146*, 662–669. [CrossRef]
52. Rodriguez, A.; Ovejero, G.; Mestanza, M.; Garcia, J. Removal of dyes from wastewaters by adsorption on pillared clays. *Ind. Eng. Chem. Res.* **2010**, *49*, 3207–3216. [CrossRef]